Contents lists available at ScienceDirect

Remote Sensing of Environment

Evaluating irrigation status in the Mekong Delta through polarimetric L-band SAR data assimilation

Hironori Arai [a,b,*], Thuy Le Toan [a], Wataru Takeuchi [c], Kei Oyoshi [d], Tamon Fumoto [e], Kazuyuki Inubushi [f]

[a] Centre d'Etude Spatiale de la BIOsphère-Université Paul Sabatier-Centre National de la Recherche Scientifique-Institut de Recherche pour le Développement-Centre National d'Etudes Spatiales (CESBIO-UPS-CNRS-IRD-CNES), 18 av. Ed. Belin, 31401 Toulouse CEDEX 9, France
[b] Japan Society for the Promotion of Science, Chiyoda, Tokyo 102-0083, Japan
[c] Institute of Industrial Science, The University of Tokyo, Meguro, Tokyo 153-8505, Japan
[d] Earth Observation Research Center, Japan Aerospace Exploration Agency, Tsukuba, Ibaraki 305-8505, Japan
[e] National Agriculture and Food Organization, Tsukuba, Ibaraki 305-8517, Japan
[f] Graduate School of Horticulture, Chiba University, Matsudo, Chiba 271-8510, Japan

ARTICLE INFO

ABSTRACT

For sustainable food production in the Mekong Delta, local information on irrigation status is essential for allocating water resources efficiently at the community level. ALOS-2 PALSAR-2 L-band SAR can be used to detect submerged and nonsubmerged soil covered by rice plants at a spatial resolution compatible with field observation but a low temporal resolution. In this study, a new multiscale data assimilation technique is developed to estimate the spatiotemporal dynamics of field water levels at a temporal resolution appropriate to inform decision-making on when to initiate irrigation. The method employs an irrigation model based on parameters representing farmers' irrigation practices. ALOS-2 PALSAR-2 data are used to derive the hydrological parameters of the model, including an irrigation parameter representing how deep the field water level dropped until the next round of irrigation was initiated. We developed observation operators for the soil submersion status under vegetation and spatial submersion percentages instead of assimilating soil moisture products. The study uses ALOS-2 PALSAR-2 data (25–100 m spatial resolution, approximately every 42 days) over the Mekong Delta and experimental data collected in situ for model initialization and validation. The estimated irrigation parameter controlling the maximum depth of field water level showed spatio-temporal consistency with the ground-observed value (RMSE = 4.24 cm). The values of the parameters also showed spatial consistency with respect to DEM data; he paddies with low irrigation model parameter values were prone to be located in low-elevation zones (<2 m), whereas high model parameters values tended to be located in paddies in the high-elevation zones (>3 m).The results show promising applications using L-band SAR observations for monitoring paddy field water level, for irrigation practices and for estimation of the water consumption and of methane emissions.

1. Introduction

The objective of this study is to develop a SAR-based monitoring system that provides daily paddy field water level data for irrigation management, required in the simulation of GHG emissions and rice productivity. In Asia, rice is the most important staple food, providing an average 32% of total calorie uptake (Maclean et al., 2002). About 90% of the global paddy area and annual output of rice production are concentrated in monsoonal Asia (FAOSTAT, 2022). Approximately 75% of global rice production is produced in irrigated lowlands encompassing delta basins in Asia, such as the Mekong, Irrawaddy, Chao Phraya, and Bengal Rivers (Barker et al., 1985; Maclean et al., 2002). To meet the increasing food demand derived from global population growth, rice cropping in the region is becoming more intensive with the use of

double/triple rice cropping techniques (FAO, 2020). However, rice production requires large amounts of water (3000–5000 L kg^{-1} rice, IRRI, 2001) and has become a major source of the potent greenhouse gas methane, approximately 11% of anthropogenic methane emissions come from rice paddy submerged soils (IPCC, 2013). Therefore, water-saving irrigation practices that have the potential to mitigate methane emissions by oxidizing the soil environment, such as alternate wetting and drying (AWD), are desirable for dissemination in this region to ensure sustainable water demand while lowering greenhouse gas emissions.

AWD is an intermittent irrigation technique to lower the amount of water used for irrigation without a significant loss of rice productivity (Bouman et al., 2007; Lampayan et al., 2015). This approach consists of temporarily suspending irrigation until the paddy soil becomes dry/oxidized. Initially, irrigation water is applied to obtain flooded conditions (5–10 cm of water above the soil surface). Then, after a certain number of days have passed, the field water level drops below the soil surface. The next irrigation is scheduled before the soil becomes dry. However, the perception of soil dryness and consequently the number of days between 2 irrigations varies widely among farmers and sites (from 1 day to >10 days) depending on the soil texture (clay/silt/sand content), percolation rate, precipitation and evaporation (Bouman et al., 2007, Lampayan et al., 2015). Various soil drought indexes have been used for scheduling irrigation (Bouman et al., 2007); for example, the soil matric potential is used to define the value of the soil drought index as the irrigation criterion. Scientists have also advocated for the use of the farmer-determined water level has also been suggested (hereafter referred to as D$_{before\_irrigation}$, i.e., how deep the field water level drops before the next round of irrigation is initiated). This specific water depth has been widely used by policy makers regarding irrigation activity, as rice farmers can easily monitor this value (Bouman et al., 2007; Rejesus et al., 2011). To define D$_{before\_irrigation}$, several field experiments have been conducted in Asia (e.g., Arai et al., 2021; Belder et al., 2004; Bouman and Tuong, 2001; Lampayan et al., 2015). These studies report that increasing the interval between rounds of irrigations to allow the field water level to drop to deeper soil layers is a promising technique to save water, reduce methane emissions and increase rice yield in the Mekong Delta (Arai, 2022). 'Irrigation when the field water level has leached 15–20 cm below the soil" is the criterion suggested by the International Rice Research Institute (IRRI). In Vietnam, in particular the Mekong delta, highly intensive cropping system was developed based on the construction and upgrading of a multilevel dike system, allowing double and triple rice crop per year. The AWD practices have also been adopted in certain regions as a water saving regulation.

However, despite the wide adoption of AWD, the values of D$_{before\_irrigation}$ differ by location (Ishido et al., 2016; Taminato and Matsubara, 2016). Most importantly, the adoption of AWD by farmers is constrained by several social/infrastructural factors. These factors include distance from the irrigation canal/drainage, density of subcanals inside the dikes, and location of pump ownership (Yamaguchi et al., 2017). At such community scale (i.e., 10-100 m spatial resolution with daily temporal resolution), heterogeneity is caused by nonsynchronized intermittent drainage in adjacent rice paddies, in land surface elevations and in cropping calendars (Dang et al., 2016; Evers and Benedikter, 2009; Miyashita et al., 2016). Other natural factors arise, such as irregular daily field water level dynamics of the irrigation canal due to ebbs and flows of tides (Wassmann et al., 2004).

These heterogeneous water management practices cause difficulties in monitoring/verifying mitigation measures operations (e.g., AWD). Such monitoring is required for irrigation management, such as allocation of irrigation/drainage canals and pumping apparatuses for irrigation/drainage schedule synchronization, opening/closing schedules of water gates attached to each dike surrounding rice paddies, dike heightening, selection of paddies that require field water level observations, etc.

In this context, there is a need to monitor the irrigation status [i.e.,

field water level dynamics and farmers' irrigation practices (e.g., D$_{before\_irrigation}$)] to evaluate the actual dissemination status of water-saving irrigation activities by each stakeholder and verify the longevity of already implemented mitigation measures. To address this issue, various studies have been conducted using remote sensing techniques to evaluate the soil submersion status. Using optical data, the rice paddy covered with water can be distinguished at the beginning of the season based on the reflectance of the water surface. The method often uses the normalized difference water index (NDWI) and the normalized difference vegetation index (NDVI) from remote sensing images to depict the differences between rice paddies and nonrice paddy areas (Zhang et al., 2020). However, as soon as the rice paddy is covered by vegetation, it is no longer possible to detect flooded and nonflooded paddy fields. Using SAR data with penetration capability, soil submersion/nonsubmersion is expected to be detectable in rice paddies for a longer period during the rice growth stage, depending on the SAR wavelength. Using C-band SAR data, Lam-Dao (2009) reported that soil submersion could be detected up to 20 days after sowing using the HH backscattering intensity of Advanced Synthetic Aperture Radar (ASAR). Using longer-wavelength SAR data with deeper penetration in the vegetation layer, Arai et al. (2018) demonstrated the performance of quadruple/dual-polarimetric L-band SAR (ALOS-2 PALSAR-2: Advanced Land Observing Satellite-2/ Phased Array type L-band Synthetic Aperture Radar-2) data to distinguish submerged paddies and nonsubmerged paddies across all rice growth stages. However, the high resolution polarimetric images cover limited area (40 km swath) and irregular temporal frequency. For larger region, ScanSAR data are more adapted. However, the 42-day repeat cycle by which PALSAR-2 ScanSAR data are acquired is not sufficient to monitor the temporal dynamics of paddy field water levels. Future L-band SAR missions, such as ALOS-4, ROSE-L and NISAR, will have 14- and 12-day repeat cycles, respectively, will be still not sufficient for temporal monitoring. Many hydrological simulation studies (e.g., Al-Yaari et al., 2014; Ines et al., 2013; Montzka et al., 2011) applying data assimilation (hereafter, assimilation) have used high temporal resolution passive microwave radiometer data [e.g., Soil Moisture and Ocean Salinity (SMOS), in which the L-band (1.4 GHz) data are collected every 3 days]. However, their spatial resolution of 20–50 km is not adapted to the heterogeneity of the rice paddies in Asia. In this regard, it is very important to develop a technique using high spatial resolution SAR data at low temporal resolution to simulate the temporal dynamics of the irrigation status of rice paddies.

The objective of this study is to develop a system that provides daily field water level data for irrigation management at the community scale. The starting point is the use of ALOS-2 PALSAR-2 data which provide pixel-based information on submersion status of paddy fields every 42 days. We prepared a model simulating field water level dynamics, based on knowledge of the hysteresis of the soil water retention curve and our long-term ground observation data. and we use the SAR data to optimize model parameters. To estimate the values of D$_{before\_irrigation}$ at the community scale, we assimilate the backscattering coefficient of the ALOS-2 PALSAR-2 data by preparing a pixel-based observation operator to detect the submersion status of paddy fields. To solve the filter divergence issues that become critical due to the low temporal resolution of satellite observations, we designed a focal statistics-based observation operator to evaluate the temporal submersion percentage and the spatial submersion percentage in a focal analysis window.

2. Methodology

In field water level simulation at local scale, soil properties and farmers' irrigation practices need to be considered. Unfortunately, most models simulating hydraulic states of agricultural soils require the field water level data as "forcing" input data (e.g., "depth of water retention layer" as input data of DNDC-rice model: Fumoto et al., 2008; Soil, Water, Atmosphere and Plant model: Govindarajan et al., 2008). The difficulty is mainly due to large uncertainties linked to anthropogenic

activities (e.g., irrigation/drainage schedule, management of tidal irrigation dikes, cropping calendars). In addition, perturbation of the ground water table caused by irregular dynamics of tidal movement of the canals also contribute to uncertainty (Arai et al., 2022; Hong et al., 2014). However, because most paddy soils over the delta are heavy clay soils characterized by a low percolation rate (Dang et al., 2016; Evers and Benedikter, 2009; Ishido et al., 2016), the soil-matric potential is expected to be the major factor controlling the states of soil water

energy. Therefore, it is expected that realistically simulating irrigation status is still possible by parameterizing these local soil properties with ground observation data relating on field waterlevel dynamics. The model is then run by assimilating SAR data simultaneously to adaptively optimize the parameters representing irrigation practices through the simulation on every pixel.

As the common water management practice in the region, soil water saturation was maintained for one week after sowing, and the paddies
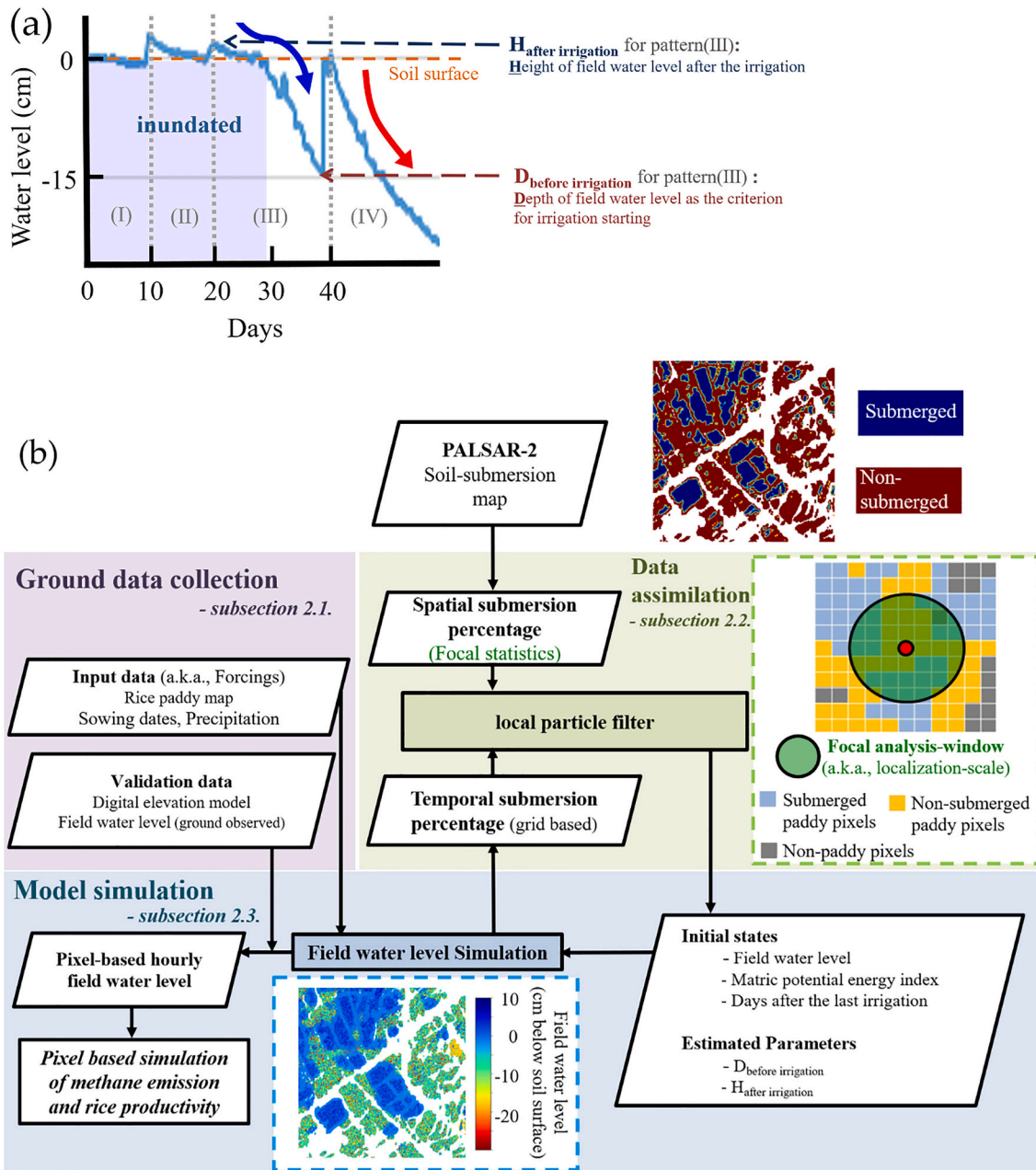
Fig. 1. Graphical explanations of the estimated model parameters by data assimilation, including $D_{before\_irrigation}$, are depicted in subfigure (a) and the flowchart outlining the different steps of the study (b). The purple box indicates ground data collection. The green box indicates the data assimilation processing. The blue box indicates the model simulation. Details of each procedure are described in the Methodology subsections. Subfigure (a) illustrates a sample of observed field water level dynamics consisting of 4 typical patterns (I-IV): (I) soil water saturation management: water level is above 0 cm; (II) continuously inundated: water level is simulated higher than 0 cm above the soil surface; (III) intermittent irrigation after submerged status (i.e., saturated soil): temporal dynamics of field water level shows an upward convex pattern with a slow dropping rate due to soil water desorption (shown as a bold blue line); and (IV) intermittent irrigation after non-inundated status (i.e., unsaturated soil): temporal dynamics of field water level shows a downward convex pattern with fast dropping rate due to soil suction (shown as a bold red line). Two model parameters representing irrigation practices (i.e., $D_{before\_irrigation}$ and $H_{after\_irrigation}$; unit: cm) for pattern (III) are illustrated. These illustrations will also be further explained in the Subsection 2.2. The boxes with broken lines in subfigure (b) are illustrations of an example of the submerged/nonsubmerged rice paddy map (top right), the analysis window (top left) and the simulated pixel-based map of the field water level (bottom). (For interpretation of the references to colour in this figure legend, the reader is referred to the web version of this article.)

were then flooded for one week to prevent weed germination. Irrigation practices consist in supplying water to a level of approximately 5 cm above the soil. In continuous flooding (CF) paddies, irrigation is repeated to maintain the 5 cm water level. In the AWD paddies, irrigation was halted 2 weeks after sowing until the next fertilization time or until the water levels in the paddies dropped to a 15-cm depth. During the flowering period (10 days from the heading date, the first day when 5% of the total number of spikes have headed), the field was maintained under continuous flooding to prevent spikelet sterility. Finally, most paddies were drained 2–3 weeks before the rice is harvested.

To realize stable L-band SAR data assimilation for field water level simulations and parameter optimization, several difficulties derived from the unique characteristics of ALOS-2 PALSAR-2 ScanSAR observations at 42-day observation repeat must be resolved: (1) the need to consider local irrigation activities (2) the low temporal resolution of satellite data (3) the need to estimate field water level for each pixel, 4) the development of a robust uncertainty quantification scheme.

To satisfy these conditions, the data assimilation system development was conducted following 5 key steps: (1) preparing a high spatiotemporal resolution model and its SAR data assimilation module,; (2) developing observation operators for soil submersion maps derived from L-band SAR data to update not only relatively short-term "fast" state variables (i.e., field water level in this study) but also long-term "slow" model parameters representing farmers' irrigation practices; (3) applying a local particle filter with an adaptive model parameter optimization scheme (4) comparison of the estimated model parameters and updated state variables with ground-observed data at each region of interest (ROI). A flowchart of this study is illustrated in Fig. 1.

2.1. Site description and ground data collection

We prepared ground observation datasets obtained at six sites (A-E) located in six different districts in the VMD (Appendix A, Fig. S1). Site A is located in Can Tho Province, and sites B-E are located in An Giang Province. The sites have been studied in previous research works: Site A: Thot Not, Can Tho [10°10′N, 105°33′E; Arai et al., 2015; Arai et al., 2018; Hong et al., 2014, Arai et al., 2021, 2022, Arai, 2022]; Site B: Chau Thanh [10°16′N, 105°08′E; (Ishido et al., 2016; Taminato and Matsubara, 2016)]; Site C: Cho Moi [10°25′N, 105°27′E; (Ishido et al., 2016)]; Site D: Thoai Son [10°16′N, 105°08′E; (Ishido et al., 2016)]; and Site E: Tri Ton, An Giang [10°23′N, 105°05′E; (Ishido et al., 2016)]. The soil at all sites is alluvial soil; classified as silty clay fluvisol at site A-C, while the soil at sites D and E is classified as sulfuric humaquepts. Site C is located on a bank adjacent to the main Mekong River (i.e., Hau River). Rice paddies at site A are surrounded by a semidike system, where the rice paddy is deeply submerged during the flood season. Rice paddies at sites B-E are surrounded by a full-dike system. Thirty rice paddies in site A and 5 rice paddy fields each at sites B-E were chosen as the ROIs (Table S1), where we installed field water level monitoring equipment. At the center of each ROI, field water-level data were collected with a water level gauge (daily, 10:00 AM-12:00 PM, at sites B-E) from November 2015 to February 2017 or with a HOBO CO-U20 L-04 water level data logger (Onset Computer Corporation, United States; collected hourly at site A) from November 2011 to March 2017 (e.g., Arai et al., 2021; Arai, 2022). At the same time, we collected information about the history of field operations (e.g., fertilization and land preparation/ sowing/harvesting dates) for each ROI throughout the observation period. Although AWD irrigation practices were conducted by farmers in most of the paddies that contained ROIs, some of the ROIs were located on paddies where the soil was continuously inundated throughout the year and data were collected by local farmers. Data assimilation and simulation were conducted all over the Mekong Delta; making use of ALOS-2 PALSAR-2 data listed in appendix Table S2.

2.2. L-band SAR data-based soil submersion map preparation

PALSAR-2 data in ScanSAR mode and polarimetric mode were used in the study. PALSAR-2's ScanSAR datasets cover the entire Mekong Delta (approximately 25–100 m spatial resolution depending on local incidence angles, dual polarization [HH/HV], Lv. 1.1; 350.5 km observation width, 355 km observation length; 105 scenes; October 2014–December 2017, appendix Table S2). Polarimetric datasets are over the region encompassing the test areas (4.3 m azimuth resolution and 5.1 m range resolution at a 37° incidence angle, quadruple polarimetry, Lv. 1.1; 40–50 km observation width, 70 km observation length; 23 scenes; November 2015–October 2016, appendix Table S2). The polarimetric data were decomposed to characterize the microwave scattering components in inundated, semi_inundated and non-inundated paddy soil (i.e., field water level of the target ROI is respectively over 0 cm above the soil surface, between 0 to −5 cm below the soil surface and lower than −5 cm below the soil surface), under different rice growth stages. The polarimetric data were converted to a coherency matrix, applied to a refined Lee filter (7 × 7 window) to reduce speckle noise, and then decomposed with 7 component decomposition (Singh et al., 2019). The ScanSAR data were processed for rice pixel detection and for soil submersion using the correction method considering local incidence angle difference as described in Arai et al. (2018). In the resulting map, the values of submerged paddy pixels were set to "1", and non-submerged paddy pixels were set to "0".

2.3. Preparation of a model simulating field water level

To convert SAR based soil submersion data into information related to field water level and irrigation activities through the data assimilation, we designed an irrigation model whose parameters are adaptively optimized by the SAR data.

For the local-scale simulation with large ensemble numbers without sacrificing the high spatial resolution of SAR data, we designed a model with low degrees of freedom for the low-cost and flexible data assimilation system. The advantages of this irrigation model are as follows: (1) all model parameters are updatable through data assimilation with up-to-date satellite data or optimizable locally with ground observation data using hierarchical Bayesian schemes with Monte Carlo methods; (2) the major factors controlling the field water level simulation are considered, including anthropogenic activities (i.e., irrigation timing/ duration and drainage) as the model parameters; and (3) the adaptive simulation of hydrological status with a carbon-nitrogen biogeochemical models.

The irrigation model simulates the field water level lowering dynamics, designed as a logit function-like behavior with the following 3 phases (Tuller, 2005) (1) Gravitational potential energy-dependent phase immediately after each irrigation event, in which the rate of water level decline is negative and relatively high since the pressure potential of the water is high due to irrigation. In addition, the soil matric potential has high negative values since the soil is relatively dry before irrigation. (2) Soil swelling/saturation phase, in which the rate of water level decline becomes relatively slow as the soil becomes wetter and swells after irrigation. In this phase, the soil matric potential becomes low due to saturation, and the pressure potential also decreases due to soil swelling. (3) In the soil suction phase (as the unsaturated soil zone is well developed, the soil matric potential becomes higher, leading the water from the saturated zone moving to the unsaturated zone, accelerating the field water level lowering. These field water level dropping dynamics are expressed with a sigmoid function in Eq. (1), referring to sigmoid-shaped soil-water physical characteristics (Appendix D).

$$\frac{d}{dt}(wl) = \frac{a - \frac{d}{dt}[sig(mp \times t - gp)]}{a} \tag{1}$$

where $\frac{d}{dt}(wl)$ is the rate of field water level decline, t is time, $sig()$ is a sigmoid function, $exp()$ is an exponential function, mp is an intensity index of matric potential, gp is an intensity index of gravitational potential, and a is a model parameter. Matric potential parameterization is conducted based on the hysteresis of the soil submersion status, as indicated by the linear combination shown in Eq. (2).

$$mp = exp(0\_1ns) \times [\alpha 1 \times (1to3ns{-}0to1ns+1)$$
$$+ \alpha 2 \times (3to7ns{-}1to3ns+1) + \alpha 3 \times (7to14ns{-}3to7ns+1)]/2 + \alpha 4 \qquad (2)$$

where 0_1ns is the temporal nonsubmersion rate (nonsubmerged number of hours/total hours during a certain period) 0–1 days before the last irrigation, $1to3ns$ is the temporal nonsubmersion rate 1–3 days before the last irrigation, $3to7ns$ is the temporal nonsubmersion rate 3–7 days before the last irrigation, and $7to14ns$ is the temporal nonsubmersion rate 7–14 days before the last irrigation. α1–4 are model parameters. Gravitational potential parameterization is conducted based on the hysteresis of the soil submersion status, as shown in Eq. (3).

$$gp = ln\Big(\beta \times \Big(H_{after\_irrigation} + \text{cum}.rain\Big)\Big) \qquad (3)$$

where $H_{after\_irrigation}$ is the field water level (cm) immediately after the last irrigation. Cum.*rain* is the cumulative precipitation (cm) since the last irrigation. β is a model parameter. How to run the model is described in Appendix D.

The model parameters a1, a2, a3, a4, β, and γ in Eqs. (2–4) are parameterized using hierarchical Bayesian modeling analyses with the Hamiltonian Monte Carlo method (Stan Development Team, 2017) based on the ground observation field data as described in Section 2.1 and Arai et al. (2018), although the temporal integration modeling scheme and observed field water level values are nonlinear, the model parameters estimated by the hierarchical Bayesian scheme with the Hamiltonian Monte Carlo method successfully converged, as described in Appendix E, Table S3. Before the application in the data assimilation system with all the training data, the performance accuracy of the validation results is confirmed ($r = 0.62$, $n = 10,080$ total, an example is illustrated in Appendix E, Fig. S2). Through the validation simulation, precipitation data and rice cropping calendar (i.e., sowing date/harvest date) and irrigation information (i.e., irrigation date, $H_{after\_irrigation}$) are used from the ground-observed data. For the ensemble simulation, we used spatially constant parameters over the Mekong delta in this study.

2.4. Data assimilation scheme with a local particle filter

The local particle filter is an advanced particle filtering technique based on the philosophy of the localization scheme of the local ensemble transform Kalman filter (Hunt et al., 2007). "Particle" has the same meaning with "ensemble member" of ensemble Kalman filter (i.e., multiple simulation with perturbations on variables or model parameters). The technique is implemented to decrease the number of required ensembles for high-dimensional systems (Potthast et al., 2019). To stabilize the assimilation system by avoiding the occurrence of filter divergence, we developed a dual-scale data assimilation scheme by implementing a focal analysis scheme as the spatial localization into the particle filtering system. The scheme allows us to assimilate not only the instantaneous state variable but also temporally cumulative state variables. A four-dimensional filtering technique with temporal localization is implemented as described in Hunt et al. (2004). The window length is set with 3 sequential observation datasets in the same observation window. Each observation is assimilated twice during the 2 sequential observation filter cycles (hereafter, repetitive cycling) to compensate for the low temporal localization of SAR datasets. Initial states in each ensemble were prepared by 2 years of spin-up running with multiplied random values for $D_{before\_irrigation}$ (mean: −15 cm; standard deviation: 7.5 cm) and $H_{after\_irrigation}$ (mean: 5 cm, standard deviation: 2.5 cm).

Field-based simulations of the water level in paddies are difficult to conduct due to heterogeneity among adjacent paddies, as stated in the introduction. However, knowing the spatial percentage of the submerged area, it is possible to derive useful a priori information related to the soil submersion probability from satellite observation data, and the temporal percentage represents the historical information at the pixel level (Aires, 2020). Field water level differences among adjacent rice paddies influence the reduction rate of the field water level (Janssen and Lennartz, 2008, 2009; Tuong et al., 1994). In particular, the water balance of rice paddies in lowland areas is affected by the net lateral water flow (Tsubo et al., 2007) and social/infrastructural (e.g., thickness/height of dykes or paddy bunds) factors. Arai et al. (2018) also reported that a large part of the paddies in the Vietnamese Mekong Delta are continuously submerged during the rainy season. Once the large paddies in the dike system are flooded, farmers need to pump out the water for several days to prepare the land for rice cropping. Conversely, once the soil emerges for long periods of time during the dry season in this region, the soil structure tends to shrink, and the water holding capacity decreases with an increased percolation rate compared with swelling soil in continuously submerged paddies. Therefore, in the dry season, large areas of paddies were detected as non submerged. Based on these findings, we designed the focal statistics-based observation operator by assuming that the spatial submersion percentage in the focal analysis window (Fig. 1) and temporal submersion percentage of a pixel located at the center of the focal analysis window are positively correlated (Cf Fig. 1, middle right illustration).

To verify this assumption, we investigated the relationship between the spatial inundation rate surrounding the ROI computed by the SAR data and the temporal inundation rate from the ground-observed field water level at each ROI (Fig. 2). The results confirmed the 1-to-1 linear relationship between the spatial inundation rate from the SAR data at the focal analysis window [i.e., the number of inundated pixels divided by the total pixels in a radius surrounding the pixel, as demonstrated in Fig. 1] and the temporal inundation rate computed by the simulated field water level (i.e., total inundated hours since the last irrigation divided by the total hours that have passed since the last irrigation in the ensemble space).

Ensembles with 1024 members (i.e., number of simulations with perturbations on states and parameters) for every grid in the GEORICE product were simulated for a 2-year data assimilation cycle with PALSAR-2 data. We also used a ground-collected cropping calendar data of ROI sites for data assimilation cycling. The estimated "$D_{before\_irrigation}$" values for every data assimilation cycle and historical data of the field water level time series were collected, and then $4{\times}4$ pixels of each target ROI were extracted. The mean value of the extracted 16 pixels of each ROI was compared with the ground observation data. For this purpose, the estimated "$D_{before\_irrigation}$" values and temporal local minima of the ground-observed field water level data from 10 days before each assimilation time (i.e., satellite observation date) to 10 days after the assimilation time were calculated.

A comparison of the spatial distribution of the $D_{before\_irrigation}$ values with the DEM was also carried out. All the grids covering the overlapping area of two InSAR-observation frames were analyzed with 256 ensemble members without lowering the spatial resolution of observation data and model grids. As an input cropping calendar for field water level simulation, the GEORICE product (https://www.globeo.net/georice). As DEM data to be compared, we employed the Multi-Error-Removed Improved-Terrain DEM (MERIT DEM, Yamazaki et al., 2017).

3. Results

Comparison with ground-observed inundation status and quadruple polarimetric PALSAR-2 data was carried out to design the PALSAR-2 data assimilation system (i.e., observation operator) to adaptively estimate the parameters of the irrigation model with high spatiotemporal resolution. Seven decomposition components showed clear consistency with 3 types of rice paddy inundation status [noninundated,
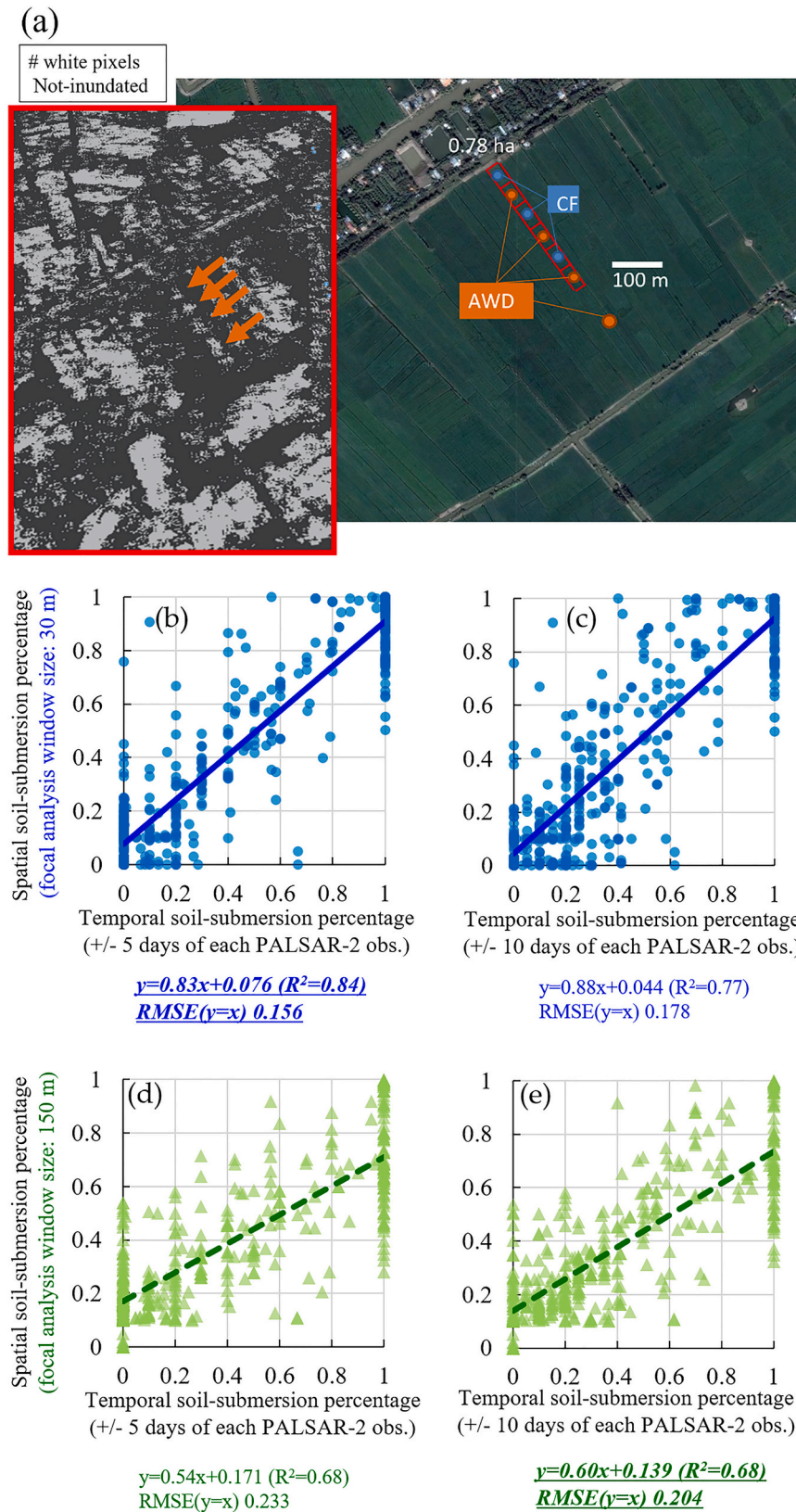
Fig. 2. A snapshot of inundation detection by PALSAR-2 obtained on one of the study sites [Site-A, Thot not, Can Tho city, Vietnam, 6th May 2016 (69 days after sowing)] with corresponding aerial photo (CF: continuously inundated paddy block; AWD: alternate wetting and drying paddy block, whose temporal water level dynamics data are presented in Arai et al., 2021) and the relationships between the temporal soil-submersion ratio calculated by the ground-measured field water level at each ROI [subfigures (b, d): +/− 5 days of each ALOS-2 PALSAR-2 observation; subfigures (c, e): +/− 10 days of each ALOS-2 PALSAR-2 observation date] and spatial soil-submersion percentage calculated by ALOS-2 PALSAR-2 data (3–6 m resolution) [blue circular points in subfigures (b, c) and green triangular plots in subfigures (d,e): all pixels of ALOS-2 PALSAR-2 polarimetric data (3–6 m resolution) within a 30 m focal analysis window and 150 m focal analysis window at each ROI, respectively].

y=0.83x+0.076 (R²=0.84)
RMSE(y=x) 0.156

y=0.88x+0.044 (R²=0.77)
RMSE(y=x) 0.178

y=0.54x+0.171 (R²=0.68)
RMSE(y=x) 0.233

y=0.60x+0.139 (R²=0.68)
RMSE(y=x) 0.204

semi-inundated paddies and inundated paddies, Figs. 3, 4, 5]. The use of all 7 components distinguished noninundated paddies from semi-inundated/inundated paddies with 1.3% cross validation error (Fig. 4a-d, Appendix F). Inundated paddies were distinguished from

semi-inundated/noninundated paddies with 12.2% cross-validation error (Appendix F). Volume scattering and other minor scattering information (Hx + OD + CD + MD where Hx: helix scattering; OD: oriented dipole scattering; CD: compound dipole scattering; MD: mixed
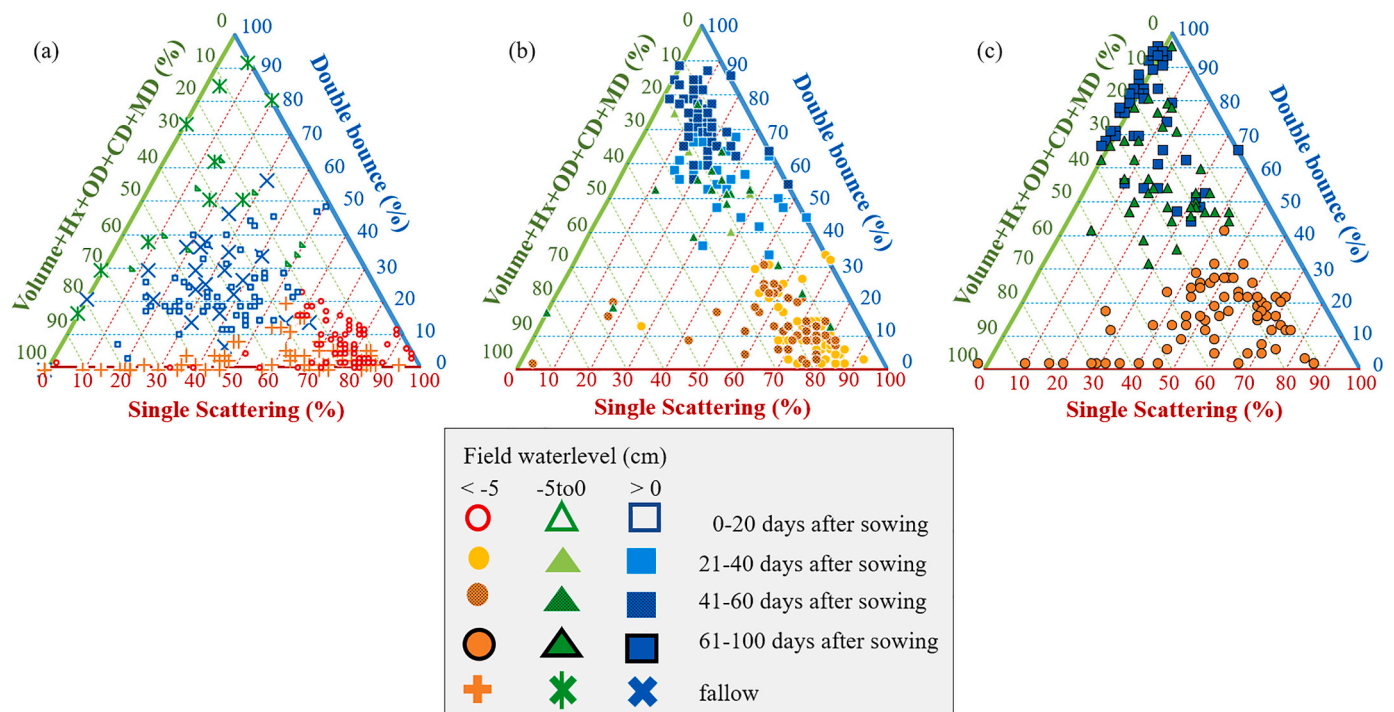
Fig. 3. Ternary plots of the intensity of PALSAR-2 scattering components produced by the Singh 7 component decomposition for 0–20 days after sowing rice paddies and fallow paddies (subfigure a), 21–60 days after sowing paddies (subfigure b), and 61–100 days after sowing paddies (subfigure c). Red, green, and blue plots indicate noninundated paddies (i.e., the ground-observed field water level of the target ROI is lower than −5 cm below the soil surface), semi-inundated paddies (i.e., the field water level is between 0 and −5 cm below the soil surface), and inundated paddies (i.e., the field water level is >0 cm above the soil surface), respectively. The number of samples in each rice growth stage group is listed in Appendix B, Table S1. (For interpretation of the references to colour in this figure legend, the reader is referred to the web version of this article.)

dipole scattering) also enabled the detection of noninundated paddies with 9.5% error, and distinguised semi-inundated paddies and non-inundated paddies with 4.5% error (Fig. 4e-g, Appendix F). Based on this information, 2 indexes were prepared as odd/(odd+double) and volume/(volume + Hx + OD + CD + MD), and the 2D-SVM (support vector machine) classification distinguished semi-inundation and non-inundation with the lowest error of 1.7% compared with the other 2D-SVM classification (Appendix F).

The HH and HV backscattering intensities of PALSAR-2 6 m resolution quadruple polarimetric data also showed different inundation classification precisions depending on the rice growth stages (Fig. 6, Appendix F). Inundated paddies were distinguished from semi-inundated paddies with 15.7% error (1.6% error for 0–20 days after sowing, 18.2% for 21–60 days after sowing, 13.5% for 61–105 days after sowing, Fig. 6, Appendix F). Noninundated paddies were distinguished from semi-inundated/inundated paddies with 23.9% error (8.7% error for 0–20 days after sowing, 19.2% for 21–60 days after sowing, 29.5% for 61–105 days after sowing, Appendix F). Non-inundated and semi-inundated paddies clearly tended to show higher HH σ^0 values than inundated paddies during 0–20 days after sowing (Fig. 6a-c). Although this trend was not clearly found during 21–60 days after sowing, HH σ^0 values tended to be greater in noninundated paddies than in inundated paddies (Fig. 6d-f). Circularly surrounding the inundated paddy plots, semi-inundated paddies tended to be distributed in the 2D scatter plot (Fig. 6, d, e). In contrast to 0–20 days after sowing stage rice groups, inundated paddies showed higher HH σ^0 values than noninundated/semi-inundated paddies (Fig. 6 g-i). Consistent with inundated paddies 61–100 days after sowing, the widely scattered distribution of high HH σ^0 value zones was also observed for the ScanSAR data.

The data assimilation system with 25 m resolution, dual-scale assimilation (pixel-based and 250 m radius) was stably run without

filter divergence at 5 validation sites with different irrigation infrastructures (i.e., a semidike system at the site-A, where paddies are submerged for approximately 2 months due to flooding every year from September to October; a full-dike system at the site-B, which comprises continuously submerged rice paddies and AWD irrigation rice paddies; a full-dike system at the site-C located adjacent to the main Hau River; and rice paddies with intermittent drainage in acid sulfate soils at the sites-D&E). In this section, we present (1) the seasonal dynamics of $D_{before\_irrigation}$ estimated at every data assimilation cycle, which is peculiar to a semidike system; (2) the spatial contrast of the updated field water level and the estimated $D_{before\_irrigation}$ observed in a full-dike system with continuously submerged rice paddies and AWD paddies; and (3) comparisons of the data assimilation outputs with ground-observed values at different sites. As preliminary experiments, 3 control experiments were conducted in a semidike system at the site-A (Appendix G, Fig. S3). The first control experiment involved normally assimilating PALSAR-2 ScanSAR data (i.e., with a focal statistics-based observation operator and variable prioritization). The second control experiment involved assimilating PALSAR-2 data without variable prioritization. The third control experiment involved assimilating PALSAR-2 data without a focal statistics-based observation operator. The comparison between the first and second control experiments showed that the PALSAR-2 data assimilation system without variable prioritization showed relatively weak/slow temporal dynamics of the estimated irrigation model parameter $D_{before\_irrigation}$ (Appendix G). This system underestimates the model parameter during the rainy/flood season and overestimates the parameter during the dry season under the current PALSAR-2 temporal resolution (Fig. S3). The third control experiment showed that the PALSAR-2 data assimilation system without a focal statistics-based observation operator could not optimize the model parameter, and the estimated value of the parameter was prone to remain constant and was unable to show seasonal dynamics (Fig. S3).
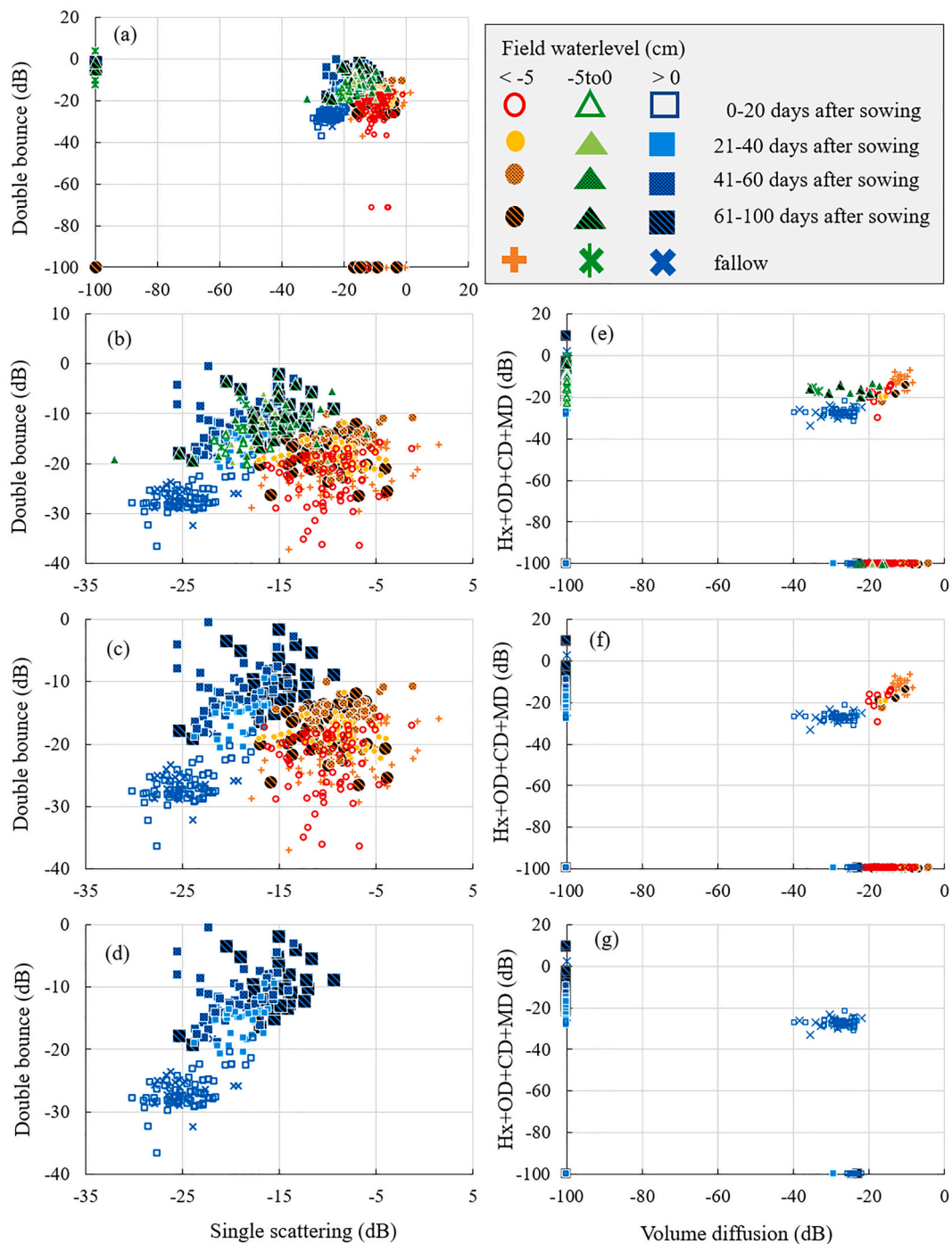
Fig. 4. Two-dimensional scatter plots of the PALSAR-2 scattering components produced by the Singh 7 component decomposition (single scattering, double bounce, volume diffusion; Hx: helix scattering; OD: oriented dipole scattering; CD: compound dipole scattering; MD: mixed dipole scattering). Red, green, and blue plots indicate noninundated paddies (i.e., the ground-observed field water level of the target ROI is lower than −5 cm below the soil surface), semi-inundated paddies (i.e., the field water level is between 0 and − 5 cm below the soil surface), and inundated paddies (i.e., the field water level is >0 cm above the soil surface), respectively. The number of samples in each rice growth stage group is listed in Appendix B, Table S1. The relationship between single scattering and double bounce is illustrated in subfigures a-d [(a) all plots, (b) all plots whose value is greater than −40 dB, (c) inundated/noninundated plots whose value is greater than −40 dB, (d) only inundated plots whose value is greater than −40 dB]. Relationships between volume diffusion and the sum of Hx, OD, CD and MD are illustrated in subfigures e-g [(a) all plots, (b) inundated/noninundated plots, (c) only inundated plots]. (For interpretation of the references to colour in this figure legend, the reader is referred to the web version of this article.)

The results obtained are illustrated in Figs. 7-10 for the site-A in a semidike system (Fig. 7) and the site-B in a full dike system, where the rice paddies inside the dike system boundaries are not submerged by flooding water (Appendix-H. Fig. S4). The temporal dynamics of field water level values obtained by ground observations at representative

ROIs (AWD paddies at the site-A/B and conventionally/continuously inundated paddies at the site-B) and spatially averaged values surrounding 16 pixels around the ROI are illustrated in Fig. 7 for the site-A and in Fig. S4 for ROIs at the site-B. The spatial pattern of updated field water level values (Fig. S4e-h, Fig. 7e-h) reflected both the soil
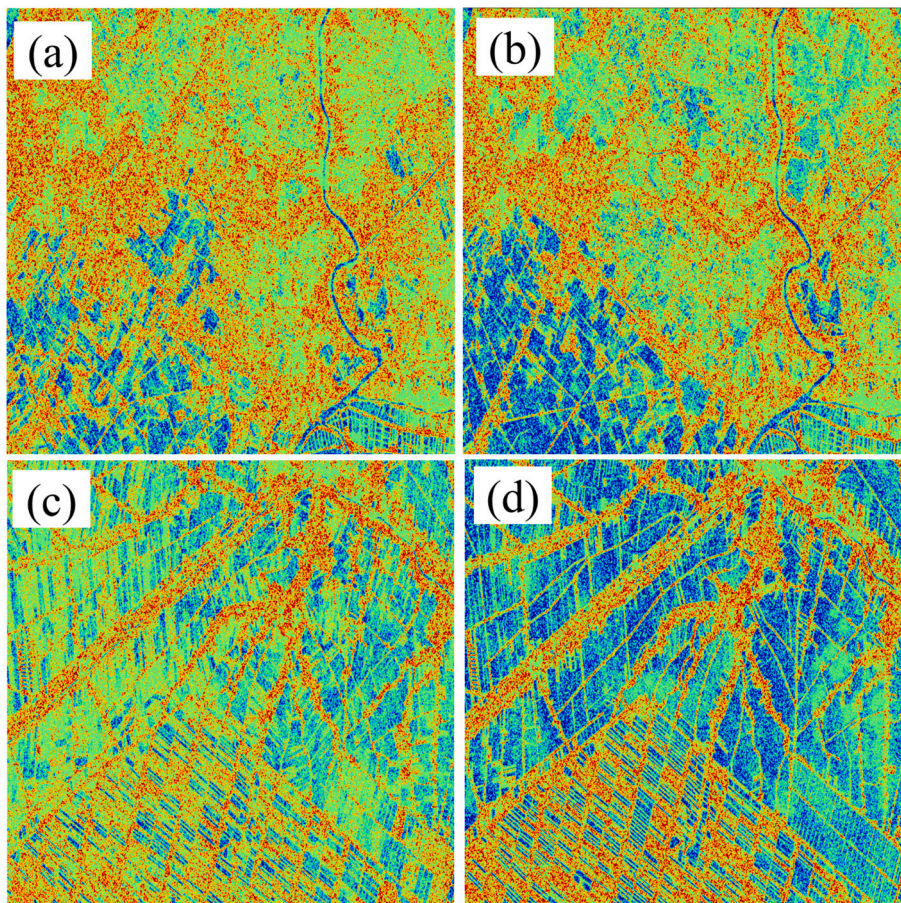
Fig. 5. Snap shots of the inundation classification images [Red: Non-inundated paddies (WL < -5 cm), Green: semi-inundated paddies (WL > -5 cm below soil surface), Blue: inundated paddies (field water level is over 0 cm above soil surface, i.e., WL > 0 cm)] based on PALSAR-2 quadruple polarimetric data obtained in An Giang province [(a) 15th June 2016 at the dry season end, (b) 10th November 2015 at the end of rainy season) and in Can Tho city [(c) 11th March 2016 at the dry season start, (b) 20th October 2017 at the end of rainy season). (For interpretation of the references to colour in this figure legend, the reader is referred to the web version of this article.)

submersion clusters detected by the focal analysis windows of the observation operator from the PALSAR-2 data (Fig. S4a-d, Fig. 7a-d) assimilated using the pixel-based observation operator and its spatial submersion percentage assimilated using the focal statistics observation operator with a dual-scale structure. Interestingly, at the site-B in the dry season (May) in 2015, low field water levels (pink pixels in Fig. S4e) were found in pixels adjacent to both non-rice pixels (i.e., along with irrigation canals). The opposite field water level patterns were found in 2016 (light blue pixels in Fig. S4e) adjacent to and non-rice pixels along with irrigation canals. This spatial pattern was derived from the spatial submersion rate along the irrigation canals, which is computed by focal statistics-based observation operators at rice pixels along with irrigation canals. This spatially high contrast among adjacent submerged paddy pixels and irrigation canals might have resulted from intense lateral water flow across dry soil with low water-holding capacity, which is derived from farmers' drainage/irrigation activities in the dry season (i. e., field water drainage from paddies to the adjacent canals in 2015 and irrigating water from the canals to the paddies in 2016).

Irrespective of the differences in observation sites, the estimated $D_{before\_irrigation}$ values and the temporally local minimum values of the ground-observed field water level showed a significant linear relationship in intermittent irrigation paddies ($r = 0.82$, $n = 282$, RMSE = 3.77 cm, Fig. 9). Although the RMSE value was relatively small in intermittent irrigation paddies (site-A: $n = 85$, RMSE = 3.68 cm; site-B: $n = 52$, RMSE = 4.09 cm; site-C: $n = 50$, RMSE = 4.26 cm; site-D: $n = 60$, RMSE = 3.33 cm; site-E: $n = 31$, RMSE = 3.45), it tended to be high at the site-B, which has relatively large continuously submerged paddies (site-B: $n = 18$, RMSE = 7.39 cm, Fig. 9). Comparison with the DEM also showed that the estimated $D_{before\_irrigation}$ values significantly decreased where triple rice cropping was practiced to a certain degree in the low-elevation zone (<2 m), particularly in the dry season (Fig. 10). In

contrast, for the triple rice cropping system area in the high-elevation zone (3 m<), $D_{before\_irrigation}$ values remained continuously high throughout the year (Fig. 10).

4. Discussion

4.1. Development of the observation operator for SAR data assimilation by developing inundation classification methodology

Inundation was classified with following 3 states as inundated paddies, semi-inundated paddies, and non-inundated paddies regarding the difference of field water level. In the studied clay soil, field water level at 0 cm of the soil surface and − 5 cm below the soil surface were differentiated by the L-band microwave signals. This indicated that L-band microwave can penetrate shallow soil surface to approximately -5 cm below soil surface. Since semi-inundated paddies was characterized by higher volume scattering and dipole scattering from rice plants (Fig. 4e), these semi-double bounce derived from the interaction between ground water table and root/stem scattering pattern was able to be detected. Though this penetration depth in the soil would be highly depending on the soil types, dielectric properties controlling states such as the soil moisture and electrical conductivity in the soil surface layer, it still has the potential to provide the information of irrigation activities such as AWD implementation status. Further development differentiating semi-inundated paddies and non-inundated paddies is expected, so that the SAR based application can provide information supporting the local scale decision making on irrigation activities more specifically in future. Non inundated paddies were distinguished by the 7 components polarimetric decomposition from semi-inundated/inundated paddies with only 1.3% cross-validation error. Although Arai et al. (2018) also reported similar results based on the Freeman–Durden method, this 7-
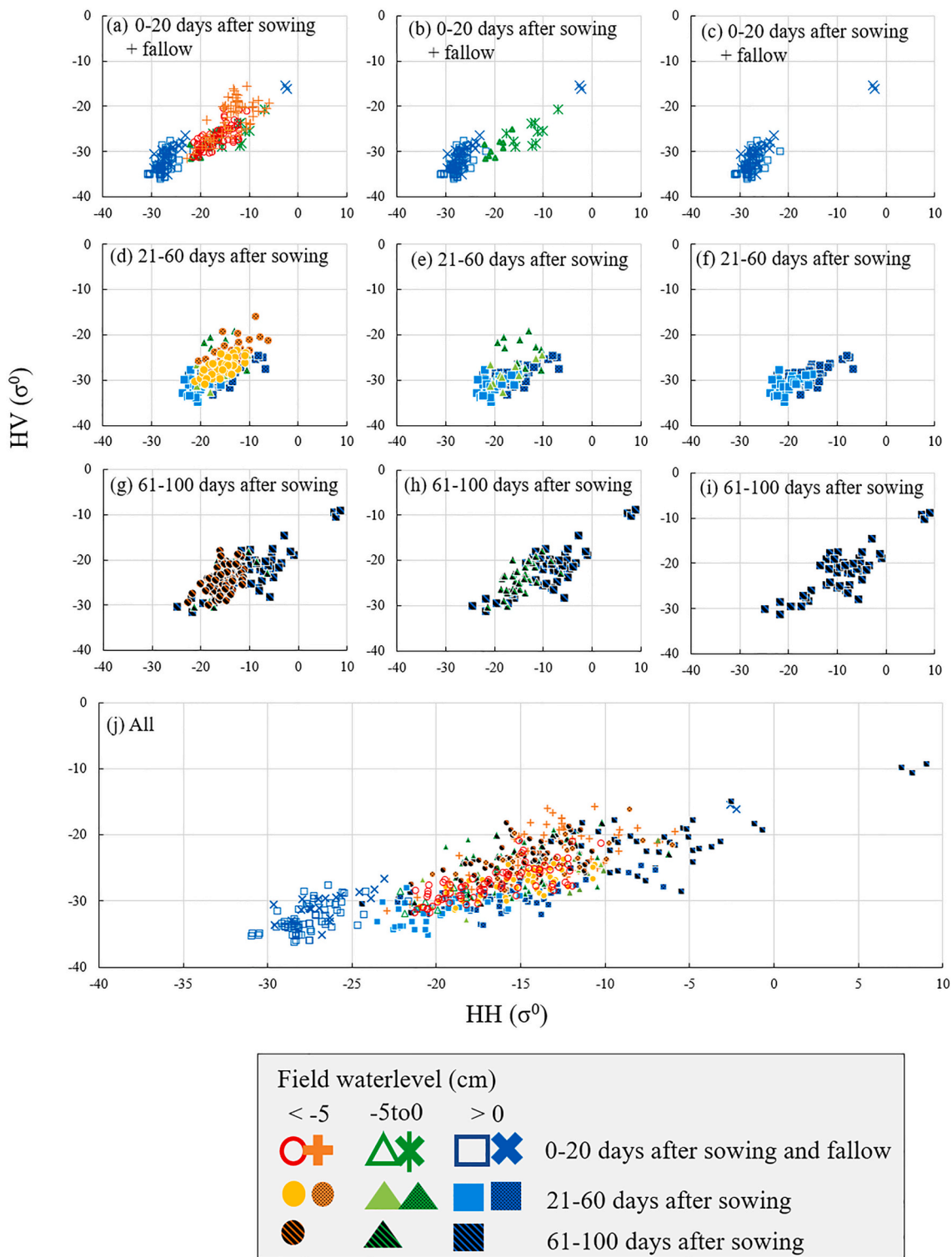
Fig. 6. Two-dimensional scatter plots of PALSAR-2 HH/HV backscattering intensities [subfigure (a-c): 0–20 days after sowing paddies or fallow paddies; subfigure (b-f): 21–60 days after sowing; subfigure (g-i): 61–100 days after sowing; and subfigure (j): all paddies]. Red, green, and blue plots indicate noninundated paddies (i. e., the ground-observed field water level of the target ROI is lower than −5 cm below the soil surface), semi-inundated paddies (i.e., the field water level is between 0 and − 5 cm below the soil surface), and inundated paddies (i.e., the field water level is >0 cm above the soil surface), respectively. Subfigures (a, d, g, j) indicate paddies with all inundation statuses. Subfigures (b, e, h) indicate semi-inundated or inundated paddies. Subfigures (c, f, i) illustrate only inundated paddies. The number of samples in each rice growth stage group is listed in Appendix B, Table S1. (For interpretation of the references to colour in this figure legend, the reader is referred to the web version of this article.)
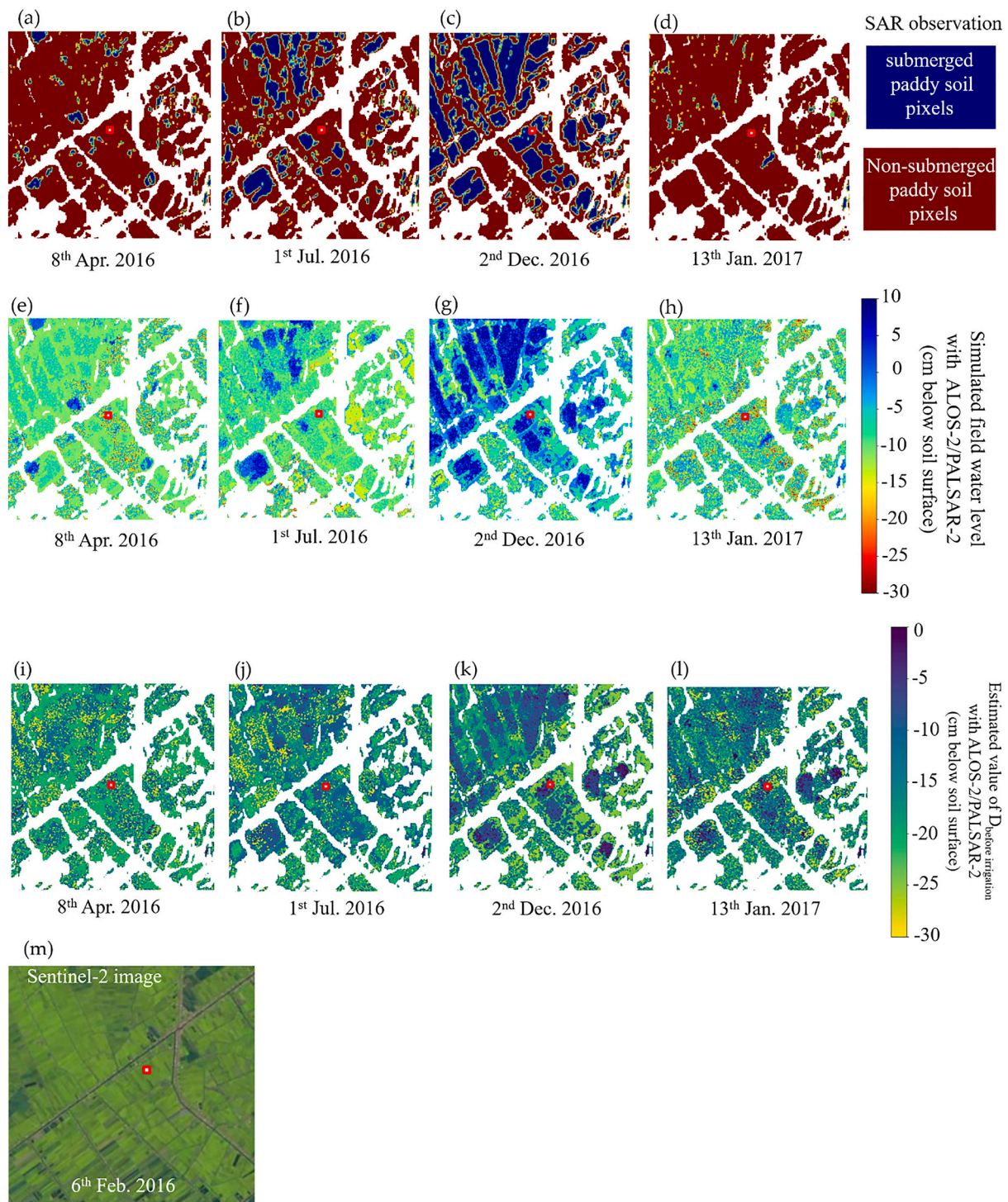
Fig. 7. Comparisons of PALSAR-2 ScanSAR observation soil-submersion/nonsubmersion map (a-d), updated field water levels (e-h) and the $D_{before\_irrigation}$ (i-l) estimated at the local particle filter steps at the site-A with a semidike system. Sentinel-2 multispectral images surrounding target sites (m). The open red squares in the subfigures indicate the location of a sample ROI whose field water level values are illustrated in Fig. 8(c). The white pixels in subfigures (a-l) indicate nonrice pixels. (For interpretation of the references to colour in this figure legend, the reader is referred to the web version of this article.)

component experiment exceeded their classification performance, with only 2.2% error using only 2 scattering components (single scattering and double bounce). More importantly, we found that semi-inundation and noninundation were distinguished by only 1.7% error based on the 2 indexes [i.e., volume/(volume + OD + CD + MD) and odd/(odd-+double)]. However, distinguishing inundated paddies from semi-inundated/noninundated paddies was carried out with a relatively high cross-validation error (12.2%). This finding indicated that

classification between inundation and semi-inundation remains a difficult problem. Although classification between semi-inundation and inundation was accomplished with relatively low error (7.3%) during 0–20 days after the sowing and fallow period, the cross-validation error was prone to become greater in later rice growing stages (Appendix F, Table S4). It was interesting to note that non-3components scattering intensities. (i.e., volume + OD + CD + MD) showed a potential to detect semi-inundated paddies ($-5 <$ WL < 0 cm below the soil surface,
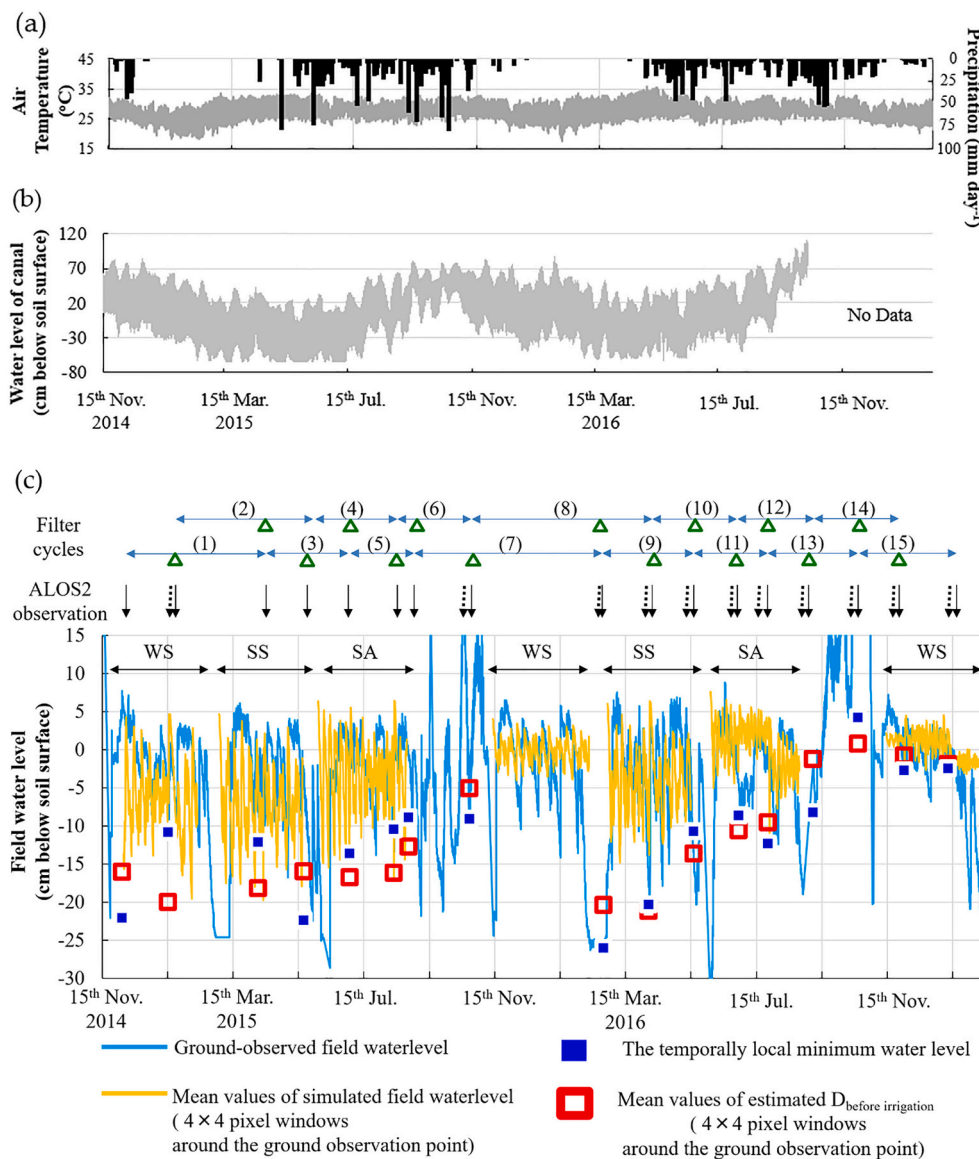
Fig. 8. A sample of the ground-observed air temperature/precipitation in subfigure (a), ground-observed water level of the irrigation canal in subfigure (b), and ground-observed field water level with a light blue line and temporally local minimum field water level adjacent to the data assimilation time (+/− 10 days of each PALSAR-2 observation) with solid blue squares in subfigure (c). The mean values of the simulated field water level during rice cropping periods (WS: winter-spring cropping; SS: spring-summer cropping; SA: summer-autumn cropping season) among 16 pixels of the ROI are shown with a yellow line, and the estimated $D_{before\_irrigation}$ by a local particle filter are indicated with open red squares in subfigure (c) at an ROI at the site-A with a semidike system. The location of the ROI is illustrated in Fig. 7 with an open red square. The length of each local particle filter window is illustrated in subfigure (c) with the assimilation order (numbers in parentheses). The ALOS-2 PAL-SAR-2 observation dates are illustrated with a downward arrow (the closed straight arrow and broken arrow indicate the difference in the observation frame) in subfigure (c).

Fig. 4e). Since methane emission in this region showed most closed relationship with the inundation period with −5 cm below soil surface (Arai, 2022), this information has a potential to evaluate regional methane emission sophisticatedly in further development.

Consistently, HH&HV σ^0 values, such as in ScanSAR mode, also showed relatively worse performance in classifying inundation and semi-inundation (8.7%–29.5%) due to the difficulty in distinguishing the difference in ground-volume interaction between inundated paddies and semi-inundated paddies. The cross-validation error of distinguishing inundated paddies from semi-inundated/non inundated paddies based on HH/HV σ^0 values became large, particularly during 21–60 days after the sowing period (18.2%; Appendix F, Table S4). To detecting inundation in this middle rice growing stages properly, polarimetric decomposition with the quadruple polarimetric data had the good performance. According to the HH/HV 2D plot (Fig. 6d-f), HH σ^0 values were not significantly differentiated between inundated paddies and noninundated paddies. However, HV σ^0 values tended to be greater in non inundated paddies than in inundated paddies during this stage due to the limitation of HV signal's dynamic range (Fig. 6d). This finding indicates that differences in volume diffusion, helix scattering or dipole scattering between inundated paddies and noninundated paddies, particularly during 21–60 days after the sowing period, are important

classification criteria that limit the performance of inundation classification performance. Since the incidence angle at the center of each scene of the quadruple observation data varied among the observation orbit-path from 27 to 37° in this study, further analysis with more ground data considering local incidence angle is desirable particularly for inundation detection of rice paddies whose rice age is 20–60 days after sowing. Further advancement of dual/quadruple polarimetric analytical methods to provide more precise signatures from HH-HV signals is also expected to overcome this limiting factor. For future application use, observation error modeling based on the distance between σ^0 values and the inundation classifying hyper-plane, which considers local incidence angle and the days after sowing will be required to improve the data assimilation performance with multi-type SAR datasets (e.g., ALOS-4, NISAR, ROSE-L, Sentinel-1).

4.2. Seasonal dynamics of $D_{before\_irrigation}$ in semidike systems and spatial dynamics of $D_{before\_irrigation}$ in full-dike systems

At the site-A, the irregular variation in the diurnal canal water level dynamics, which would influence the ground water level in the paddies, indicated the difficulty of creating 2-dimensional simulations of the paddy field water level due to the difficulty of reproducing the influence
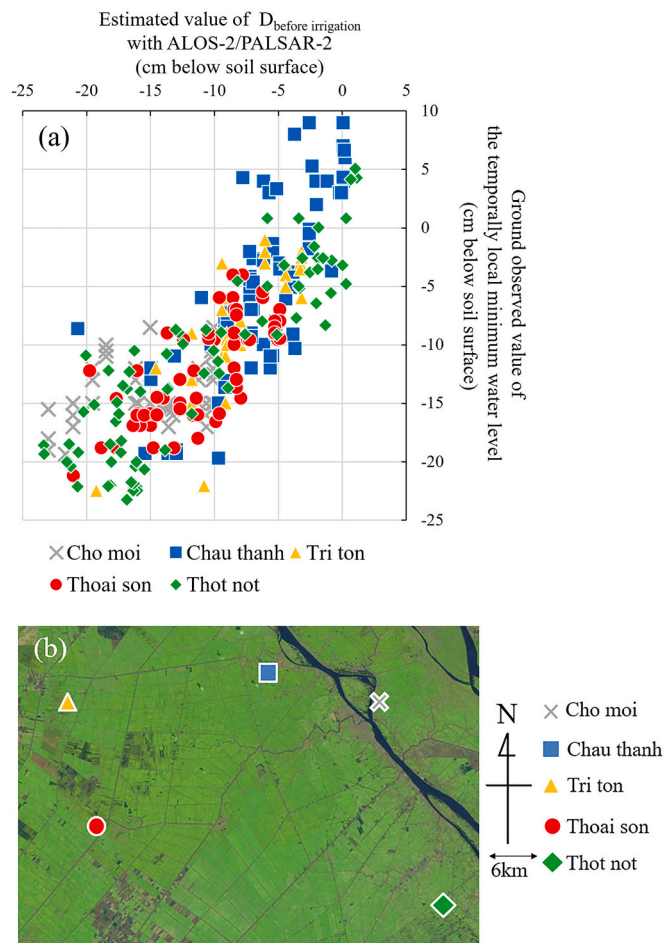
Fig. 9. Relationship between the estimated value of $D_{before\_irrigation}$ by the local particle filter and the hourly ground-monitored value of the temporally local minimum field water level adjacent to the data assimilation time (duration from 10 days before each assimilation time to 10 days after the assimilation time, averaged among 16 pixels around each ground observation point) (RMSE = 4.24 cm, subfigure a) and Sentinel-2's multispectral images surrounding target sites observed on 6 February 2016 (subfigure b).

of the ebb and flow of tides on the simulation. During the dry season from January to June, when it hardly rained and the water level of the irrigation canal significantly decreased, few soil submersion events were detected in the paddies (Fig. 4a, d), and relatively low values of field water level (Fig. 4e, h) and $D_{before\_irrigation}$ (Fig. 4i, l) were updated. As the precipitation rate and water level of the irrigation canal tended to increase, more submerged paddy pixels were detected, and high values of field water level and $D_{before\_irrigation}$ were updated (Fig. 4g, k). Although there was a relatively large discrepancy between the estimated values of $D_{before\_irrigation}$ and the ground-observed values of the temporally local minimum field water level at the beginning stage of data assimilation, the discrepancy tended to diminish as the prior spread adjusted to the true states through the data assimilation cycles (Fig. 6c). The $D_{before\_irrigation}$ value became relatively low in the annually driest cropping season [spring-summer cropping season (SS) from March to May] and high in the annually wettest season [summer-autumn cropping season (SA) from June to September] (Fig. 4, 6c). These results indicated that the $D_{before\_irrigation}$ estimated by the local particle filter has the potential to regionally evaluate the dissemination status of a safe-AWD (Lampayan et al., 2015; Rejesus et al., 2011).

In contrast to the site-A with a semidike system, seasonal dynamics were negligible at the site-B with a full-dike system (Appendix-H&I, Figs. S4 and S5). The range of the estimated $D_{before\_irrigation}$ was shorter in

the full-dike sites than that at the site-A with a semidike system, whose estimated values were widely scattered from approximately −27.6 cm to +1.0 cm, because the values are year-round stable in a full-dike system. However, dynamic spatial differences in the $D_{before\_irrigation}$ values were found at the sites with full-dike systems (Appendix-H. Fig. S4), in contrast to those at the site-A (Fig. 7). As indicated by the ground-observed field water level at the site-B, the field water level also tended to be greater in continuously submerged paddies than in intermittently drained paddies, as was the case for the estimated values of $D_{before\_irrigation}$ (Appendix-I. Fig. S5). The field water level was mostly >10 cm above the soil surface in continuously submersion-prone paddies, although the irrigation height is recommended as 5 cm to implement safe-AWD (Lampayan et al., 2015; Rejesus et al., 2011) in this region. Related to this result, a significant influence of the spatial distribution of infrastructural properties (altitude of the soil surface and distance from the irrigation canal) on the AWD adoption rate has been reported at the targeted sites (e.g., Miyashita et al., 2016; Yamaguchi et al., 2019). These results indicate that the areas with a high $D_{before\_irrigation}$ as estimated by the local particle filter also exhibit submersion-prone factors, which is consistent among all cropping seasons. Compared with the site-A, a relatively high annual methane emission reduction rate by the implementation of AWD to lower the field water level and dry the soil has been reported at the site-B [methane emission reduction rate: site-B: 49–74% (Taminato and Matsubara, 2016); site-At: 31.5–66.0% (Arai, 2022)]. The spatial contrast illustrated by the pixels with both high and low values of the estimated $D_{before\_irrigation}$ among all cropping seasons might indicate that the impact on the spatial distribution of land hydraulic behavior as affected by (or affects) the field water management status. The spatial distribution of field water levels and $D_{before\_irrigation}$ updated by the local particle filter resulted in linearly shaped borders between soil-submerged clusters (Fig. 7e-h, Fig. S4e-h), with distributions consistent with the location of subcanals for drainage and irrigation. Notably, the updated field water levels and $D_{before\_irrigation}$ tended to be lower along the subcanals. This result indicated that the dual-scale assimilation technique can detect the impacts of social factors at the community scale while also considering lateral water seepage/percolation, even when the allocation/distribution of social factors and lateral flow was not included in the simulation. At the site-B, a relatively large discrepancy between the estimated $D_{before\_irrigation}$ and the local minimum field water level of the ROI was detected when intermittent drainage was conducted during the assimilation time. The reason for this difference might be due to the relatively intense side flow, which rapidly decreases the field water level, and the results indicated that the estimation accuracy deteriorates if intense side flow with drainage occurs on the satellite observation date. To reduce the bias, frequent state updates with more frequent observation data are desirable (e.g., ALOS-4, NISAR, ROSE-L). Furthermore, the presentation of a local particle filter system assimilating new L-band SAR observation techniques with higher spatiotemporal resolution is expected to delineate finer spatial distributions of social factors and improve the system from community-scale evaluations to individual farming-scale evaluations.

4.3. Performance of the parameter estimation in the Mekong Delta

The validation of the estimated $D_{before\_irrigation}$ model parameter showed a 1-to-1 relationship (Fig. 9) with the ground-observed value of the temporally local minimum water level irrespective of the differences in observation sites, although some biased plots were found at the sites-B&C. At the ROI at the site-B, the local minimum field water level was mostly higher than the soil surface in the paddies that were prone to continuous submersion (Fig. S5). In such paddies, it was difficult for the assimilation system to adequately differentiate the values of $D_{before\_irrigation}$ when the values were >0 cm (Fig. 9). This is because of the limitation of observation operators' sensitivities, which evaluate only the difference between the soil submersion and nonsubmersion statuses (i.e., they are still unable to directly observe the field water level under
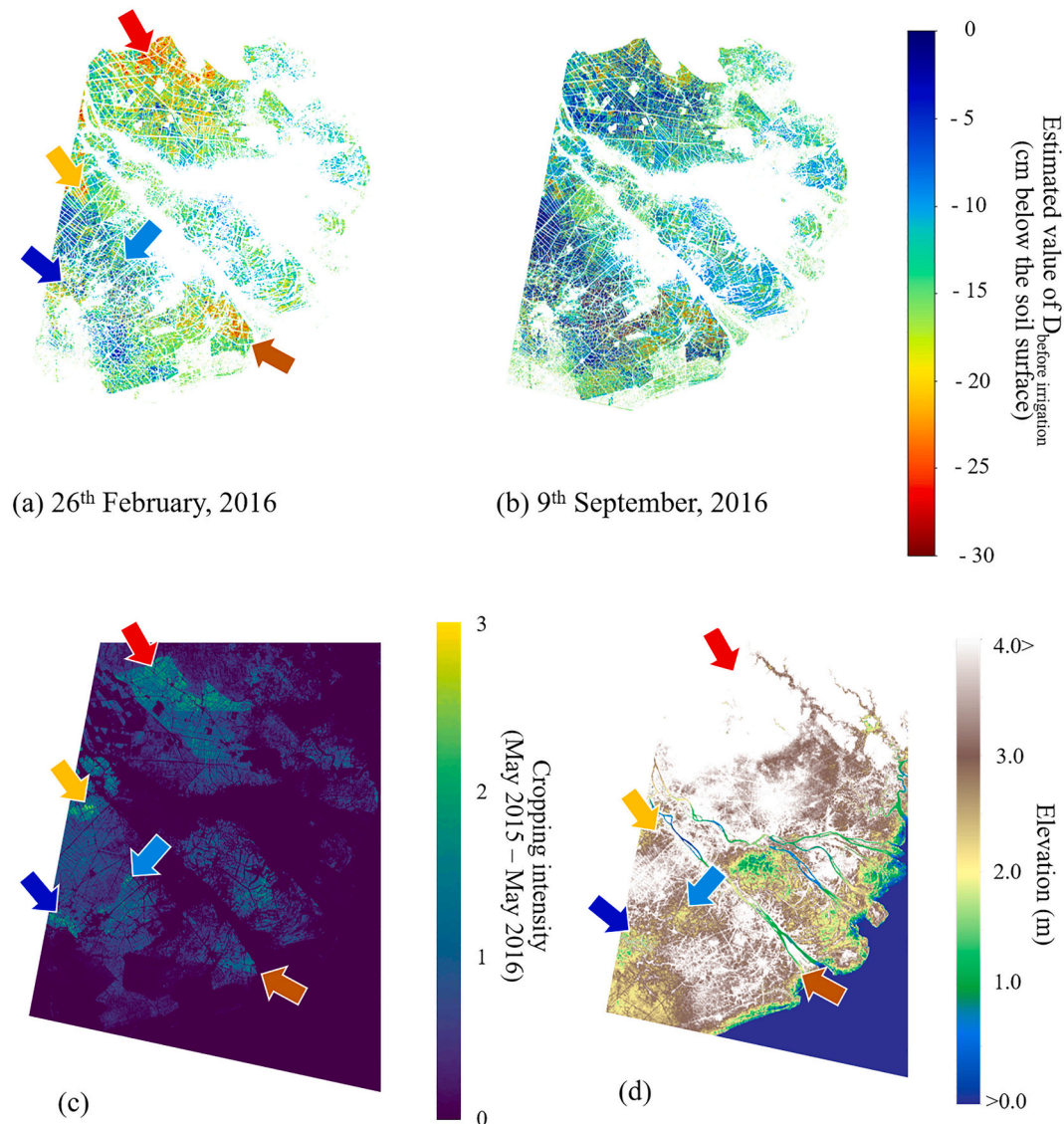
Fig. 10. Comparisons of $D_{before\_irrigation}$ estimated by the 256-member data assimilation with PALSAR-2 ScanSAR (a: 26 February 2016; b: 9 September 2016), input data of the GEORICE rice annual cropping intensity map (c), and MERIT DEM (d). Red, brown and orange indicate regions where $D_{before\_irrigation}$ values became significantly low. Blue and light blue indicate regions where $D_{before\_irrigation}$ values became significantly high. (For interpretation of the references to colour in this figure legend, the reader is referred to the web version of this article.)

the soil surface by PALSAR-2 data with the currently available algorithms). Therefore, the bias became relatively great at the continuously inundated paddies (number of ROIs whose temporally local minimum values exceeded the soil surface: 25 pixels; mean ± standard deviation of the $D_{before\_irrigation}$: 4.99 ± 2.13 cm above the soil surface; Fig. 9), where paddies were prone to continuous submersion with high field water levels (mostly >10 cm above the soil surface). Regarding the main purpose of this application, the approach presented here can provide adequate values of field water level and $D_{before\_irrigation}$ as long as the values are lower than the soil surface. Although it is still difficult for this application to differentiate continuously inundated paddies and intermittent irrigation paddies from the momentary value of $D_{before\_irrigation}$, it might detect continuously inundated paddy pixels based on time series data since the detected $D_{before\_irrigation}$ values from continuously inundation-prone paddies' ROIs were constant nearly year-round, unlike those of intermittent irrigation paddies (Fig. S5). Relatively large biases were also found at the site-C, which is located in a sandbank adjacent to the main Mekong River (Hau River, Fig. 9), due to the intense side flow of the dike system caused by large-scale irregular

temporal dynamics of the river water level as affected by the ebb and flow of the tides. As Lampayan et al., 2015 summarized from various field results obtained over Asian rice paddies, the optimum $D_{before\_irrigation}$ value is 15–20 cm below the soil surface, irrespective of differences in soil type. Arai et al. (2021) also reported that rice yield tended to be higher in rice paddies whose $D_{before\_irrigation}$ values were 15–20 cm (i.e., safe-AWD rice paddies) than in continuously submerged paddies. By spatiotemporally identifying rice paddy pixels whose $D_{before\_irrigation}$ values are 15 cm below the soil surface, this technique has the potential to map rice paddies where the $D_{before\_irrigation}$ values should be lowered by improving infrastructural/social factors as well as reducing irrigation water usage. In addition, by locally identifying rice paddies whose $D_{before\_irrigation}$ values are less than -20 cm, this technique can consistently detect the water demand or severe drought stress with high spatiotemporal resolution. Spatiotemporal identification of drainage/irrigation-required zones inside dikes with factors restricting the adoption of AWD (Miyashita et al., 2016; Yamaguchi et al., 2019) has the potential to provide useful information for stakeholders at the local community scale. Interestingly, the low-$D_{before\_irrigation}$ region was

located in the low-elevation zone (<2 m), and the high-$D_{before\_irrigation}$ region was located in the high-elevation zone (>3 m), even though we did not use the DEM for our data assimilation process. Comparison with the DEM also showed that the estimated $D_{before\_irrigation}$ values significantly decreased where triple rice cropping was practiced in the low-elevation zone, particularly in the dry season, and became high where triple rice cropping was practiced to a certain degree in the low-elevation zone continuously throughout the year. Consistent with other ground-based social science surveys, continuously submerged paddies are more common in low-elevation areas that are relatively far from dike/river systems, and elevation and the distance from a canal exhibit a statistically significant relationship with the rate of AWD adoption (e.g., Miyashita et al., 2016; Yamaguchi et al., 2019). These results indicated the necessity of spatiotemporally identifying AWD irrigation implementation, and our system has the potential to provide adequate information at both local and regional scales. With safe-AWD, it is recommended to irrigate water into paddies when the water level drops to −15 cm (i.e., $D_{before\_irrigation}$ = −15 cm) to reduce irrigation water and methane emissions from soil without sacrificing rice yield. By assimilating L-band SAR data, we estimated these field-level values before irrigation. We found that almost 50% of paddies were irrigated before the field water level dropped to −15 cm (53.0% for June 2017, 56.9% for December 2017). In particular, approximately 15% of the total rice paddies in the delta were irrigated before the water level dropped to −5 cm and nearly continuously flooded (13.8% for June 2017, 19.8% for December 2017), and approximately 33% of the total rice paddies in the delta were irrigated before the water level dropped to −10 cm (30.6% for June 2017, 35.4% for December 2017). These results indicated that the Mekong Delta still has great potential to reduce methane emissions without sacrificing rice yield. With respect to the adaptation measures for soil drought/soil salinity, we found that the measures are applied to approximately 25% of the total rice paddies in the Mekong Delta (26.2% for June 2017, 24.1% for December 2017). It is important to identify these freshwater-scarce zones and recommend a smart freshwater grid system to distribute freshwater to these zones. However, these significantly high/low values were detected only where triple rice cropping was practiced. The results indicate that higher temporal resolution SAR data, such as ALOS-4/NISAR/ROSE-L, may be essential to quantify the irrigation status, particularly for single/double cropping paddies.

The issue of methane emissions from the Mekong Delta caused by continuous fresh organic carbon supply through double/triple rice cropping into frequently irrigated paddy soil (Yan et al., 2009; Arai et al., 2022) has become a matter of concern for sustainable agroecosystem management. To operationally evaluate the methane emission status, rice yield as affected by drought stress and spatiotemporal implementation status of AWD irrigation to provide decision support and inform carbon pricing schemes, coupling the field water level simulation with methane emission simulation models is a viable approach (Fumoto et al., 2008; Arai et al., 2018). However, most hydrological or crop/soil biogeochemistry models require field water levels as input data and cannot simulate the field water level itself. By updating realistic field water level data with spatiotemporally optimized $D_{before\_irrigation}$ based on SAR data, these models could simulate rice productivities and greenhouse gas emissions such as methane by adaptatively optimizing the input of field water level on every SAR data pixel without requiring a large amount of ground-observed field water level data (Arai et al., 2022).

5. Conclusion

The concept and required techniques of SAR data assimilation with relatively high spatial resolution and low temporal resolution are demonstrated in this study. This study evaluates a soil drought index (i. e., $D_{before\_irrigation}$) that has high potential to inform decision making regarding the sustainable water and carbon resource management of rice paddies. Moreover, this approach can support adaptive simulation with biogeochemistry models considering farmer irrigation practices. By prioritizing the estimation of model parameters with long temporal scales rather than updating state variables with short temporal scales, adequate performance with improved accuracy was confirmed based on validation with ground observation datasets. Since most field-scale hydraulic simulation models for paddy soils treat field water level data as only forcing inputs, we implemented a field water level simulation scheme optimized for a high spatial resolution data assimilation system. Validation with ground observation data was conducted by taking advantage of high spatial resolution assimilation, and adequate performance of the dual-scale observation operators and model parameter estimations by local particle filter were demonstrated. The spatiotemporal dynamics of $D_{before\_irrigation}$ model parameters were detected depending on the differences in infrastructure (i.e., seasonal dynamics in a semidike system and spatial contrast between intermittently drained paddies and paddies prone to continuous submersion in a full-dike system). Although some factors causing bias remain (side flow in rice paddies that are located adjacent to a river with relatively drastic daily/ seasonal dynamics due to the ebb and flow of tides, intermittent drainage or continuous submersion management), the validation results of the dual-observation operators indicated the potential for improvement by downscaling the spatial localization and shortening the assimilation cycle by improving the linearity of the observation operators with new L-band SAR data observation techniques with increased spatiotemporal resolution (e.g., ALOS-4, NISAR, ROSE-L).

CRediT authorship contribution statement

Hironori Arai: Conceptualization, Methodology, Software, Data curation, Validation, Writing – original draft, Writing – review & editing, Visualization, Funding acquisition, Project administration. **Thuy Le Toan:** Supervision, Project administration, Investigation, Writing – review & editing. **Wataru Takeuchi:** Supervision, Project administration, Resources. **Kei Oyoshi:** Resources, Project administration. **Tamon Fumoto:** Formal analysis. **Kazuyuki Inubushi:** Resources, Investigation, Validation.

Declaration of Competing Interest

The authors declare that they have no known competing financial interests or personal relationships that could have appeared to influence the work reported in this paper.

Acknowledgments

Appendix A. Supplementary data

Supplementary data to this article can be found online at https://doi. org/10.1016/j.rse.2022.113139.

References

Aires, F., 2020. Surface water maps de-noising and missing-data filling using determinist spatial filters based on several a priori information. Remote Sens. Environ. 237, 111481.

Al-Yaari, A., Wigneron, J.P., Ducharne, A., Kerr, Y., De Rosnay, P., De Jeu, R., Govind, A., Al Bitar, A., Albergel, C., Munoz-Sabater, J., Richaume, P., Mialon, A., 2014. Global-scale evaluation of two satellite-based passive microwave soil moisture datasets (SMOS and AMSR-E) with respect to land data assimilation system estimates. Remote Sens. Environ. 149, 181–195.

Arai, H., 2022. Increased rice yield and reduced greenhouse gas emissions through alternate wetting and drying in a triple cropped rice field in the Mekong Delta. Sci. Total Environ. accepted.

Arai, H., Hosen, Y., Hong, Van N.P., Chiem, N.H., Inubushi, K., 2015. Greenhouse gas emissions derived from rice straw burning and straw-mushroom cultivation in a triple rice cropping system in the Mekong Delta. Soil Sci. Plant Nutr. 61, 719–735.

Arai, H., Takeuchi, W., Oyoshi, K., Nguyen, L.D., Inubushi, K., 2018. Estimation of methane emissions from rice paddies in the Mekong Delta based on land surface dynamics characterization with remote sensing. Remote Sens. 10 (9), 1438.

Arai, H., Hosen, Y., Chiem, N.H., Inubushi, K., 2021. Alternate wetting and drying enhanced the yield of a triple-cropping rice paddy of the Mekong Delta. Soil Sci. Plant Nutr. 2021 (67), 493–506.

Arai, H., Takeuchi, W., Oyoshi, K., Nguyen, L.D., Inubushi, K., Fumoto, T., Le Toan, T., 2022. Pixel-based evaluation of rice production and related greenhouse gas emissions in the Mekong Delta integrating SAR data and ground observations. In: Vadrevu, K.P., Le Toan, T., Ray, S.S., Justice, C. (Eds.), Remote Sensing of Agriculture and Land Cover/Land Use Changes in South and Southeast Asian Countries. Springer, Cham. https://doi.org/10.1007/978-3-030-92365-5_14.

Barker, R., Herdt, R.B., Rose, B., 1985. The Rice Economy of Asia. Resources for the Future. Johns Hopkins University Press, Washington. http://books.irri.org/0915707152_content.pdf.

Belder, P., Bouman, B.A.M., Cabangon, R., Guoan, L., Quilang, E.J.P., Yuanhua, L., Spiertz, J.H.J., Tuong, T.P., 2004. Effect of water-saving irrigation on rice yield and water use in typical lowland conditions in Asia. Agr. Water Manag. 65 (3), 193–210.

Bouman, B.A.M., Tuong, T.P., 2001. Field water management to save water and increase its productivity in irrigated lowland rice. Agr. Water Manag. 49 (1), 11–30.

Bouman, B.A.M., Lampayan, R.M., Tuong, T.P., 2007. Water management in irrigated rice: coping with water scarcity. Int. Rice Res. Inst. 53. http://books.irri.org/9789712202193_content.pdf.

Dang, T.D., Cochrane, T.A., Arias, M.E., Van, P.D.T., de Vries, T.T., 2016. Hydrological alterations from water infrastructure development in the Mekong floodplains. Hydrol. Process. 30 (21), 3824–3838.

Evers, H.D., Benedikter, S., 2009. Hydraulic bureaucracy in a modern hydraulic society-strategic group formation in the Mekong Delta, Vietnam. Water Altern. 2 (3), 416–439.

FAOSTAT, 2022. FAO Statistical Databases. URL. http://faostat.fao.org/ (accessed on 23 May 2020).

Fumoto, T., Kobayashi, K., Li, C., Yagi, K., Hasegawa, T., 2008. Revising a process-based biogeochemistry model (DNDC) to simulate methane emission from rice paddy fields under various residue management and fertilizer regimes. Glob. Chang. Biol. 14 (2), 382–402.

Govindarajan, S., Ambujam, N.K., Karunakaran, K., 2008. Estimation of paddy water productivity (WP) using hydrological model: an experimental study. Paddy Water Environ. 6 (3), 327–339.

Hong, Van N.P., Nga, T.T., Arai, H., Hosen, Y., Chiem, N.H., Inubushi, K., 2014. Rice straw management by farmers in a triple rice production system in the Mekong Delta, Viet Nam. Trop. Agr. Dev. 2014 (58), 155–162.

Hunt, B.R., Kalnay, E., Kostelich, E.J., Ott, E., Patil, D.J., Sauer, T., Szunyogh, I., Yorke, J. A., Zimin, A.V., 2004. Four-dimensional ensemble Kalman filtering. Tellus A 56 (4), 273–277.

Hunt, B.R., Kostelich, E.J., Szunyogh, I., 2007. Efficient data assimilation for spatiotemporal chaos: a local ensemble transform Kalman filter. Physica D: Nonlinear Phenomena 230 (1–2), 112–126.

Ines, A.V., Das, N.N., Hansen, J.W., Njoku, E.G., 2013. Assimilation of remotely sensed soil moisture and vegetation with a crop simulation model for maize yield prediction. Remote Sens. Environ. 138, 149–164.

IPCC, 2013. Climate change 2013: The physical sience basis. In: Stocker, T.F., et al. (Eds.), Working Group Contribution to the Fifth Assessment Report of the Intergovernmental Panel on Climate Change. Cambridge University Press, Cambridge, UK, and New York, NY, p. 1535.

IRRI (International Rice Research Institute), 2001. Annual Report. 2000–01. Rice Research: The Way Forward. Los Banos. International Rice Research Institute, Philippines.

Ishido, K., Nguyen, X.L., Taminato, T., Hosen, Y., Arai, H., 2016. Dissemination of a water-saving technology to paddy fields in the Mekong Delta. In: Annual Meeting of the Japanese Society of Irrigation, Drainage and Rural Engineering 2016. http://soil.en.a.u-tokyo.ac.jp/jsidre/search/PDFs/16cd/manuscript_pdf/[6-28].pdf (accessed on 11 April 2018) [in Japanese].

Janssen, M., Lennartz, B., 2008. Characterization of preferential flow pathways through paddy bunds with dye tracer tests. Soil Sci. Soc. Am. J. 72 (6), 1756–1766.

Janssen, M., Lennartz, B., 2009. Water losses through paddy bunds: methods, experimental data, and simulation studies. J. Hydrol. 369 (1–2), 142–153.

Lam-Dao, N., 2009. Rice Crop Monitoring Using New Generation Synthetic Aperture Radar (SAR) Imagery. Ph.D. Thesis. University of Southern Queensland, Queensland, Australia.

Lampayan, R.M., Rejesus, R.M., Singleton, G.R., Bouman, B.A., 2015. Adoption and economics of alternate wetting and drying water management for irrigated lowland rice. Field Crop Res. 170, 95–108.

Maclean, J.L., Dawe, D.C., Hardy, B., Hettel, G.P., 2002. Rice Almanac, third ed. IRRI, Los Baños, Philippines, p. 253.

Miyashita, M., Muramatsu, Y., Kawashima, T., 2016. Assessment and analyses of the reality in diffusion of water-saving irrigation technology and the constraints in diffusion of Alternate Wetting and Drying in An Giang Province, Vietnam. J. JASS 32 (2), 71–80 [in Japanese with English abstract]. http://10.14962/jass.32.2_71.

Montzka, C., Moradkhani, H., Weihermüller, L., Franssen, H.J.H., Canty, M., Vereecken, H., 2011. Hydraulic parameter estimation by remotely-sensed top soil moisture observations with the particle filter. J. Hydrol. 399 (3–4), 410–421.

Potthast, R., Walter, A., Rhodin, A., 2019. A localized adaptive particle filter within an operational NWP framework. Mon. Weather Rev. 147 (1), 345–362.

Rejesus, R.M., Palis, F.G., Rodriguez, D.G.P., Lampayan, R.M., Bouman, B.A., 2011. Impact of the alternate wetting and drying (AWD) water-saving irrigation technique: evidence from rice producers in the Philippines. Food Policy 36 (2), 280–288.

Singh, G., Malik, R., Mohanty, S., Rathore, V.S., Yamada, K., Umemura, M., Yamaguchi, Y., 2019. Seven-component scattering power decomposition of POLSAR coherency matrix. IEEE Trans. Geosci. Remote Sens. 57 (11), 8371–8382.

Stan Development Team, 2017. RStan: The R Interface to Stan, Version 2.15. Retrieved April 19, 2017, from. http://mc-stan.org/rstan.html.

Taminato, T., Matsubara, E., 2016. Impacts of two types of water-saving irrigation system on greenhouse gas emission reduction and rice yield in paddy fields in the Mekong delta. IDRE J. 84, 195–200. https://www.jstage.jst.go.jp/article/jsidre/84/3/84_I_195/_pdf (accessed on 11 April 2018) [in Japanese].

Tsubo, M., Fukai, S., Tuong, T.P., Ouk, M., 2007. A water balance model for rainfed lowland rice fields emphasising lateral water movement within a toposequence. Ecol. Model. 204 (3–4), 503–515.

Tuller, D.O., 2005. Water retention and characteristic curve. In: Hillel, D. (Ed.), Encyclopedia of Soils in the Environment, pp. 278–289. https://doi.org/10.1016/B0-12-348530-4/00376-3.

Tuong, T.P., Wopereis, M.C.S., Marquez, J.A., Kropff, M.J., 1994. Mechanisms and control of percolation losses in irrigated puddled rice fields. Soil Sci. Soc. Am. J. 58 (6), 1794–1803.

Wassmann, R., Hien, N.X., Hoanh, C.T., Tuong, T.P., 2004. Sea level rise affecting the Vietnamese Mekong Delta: water elevation in the flood season and implications for rice production. Clim. Chang. 66 (1–2), 89–107.

Yamaguchi, T., Luu, M.T., Minamikawa, K., Yokoyama, S., 2017. Compatibility of alternate wetting and drying irrigation with local agriculture in an Giang province, Mekong Delta, Vietnam. Trop. Agr. Dev. 61 (3), 117–127. https://doi.org/10.11248/jsta.61.117.

Yamaguchi, T., Tuan, L.M., Minamikawa, K., Yokoyama, S., 2019. Assessment of the relationship between adoption of a knowledge-intensive water-saving technique and irrigation conditions in the Mekong Delta of Vietnam. Agr. Water Manag. 212, 162–171.

Yamazaki, D., Ikeshima, D., Tawatari, R., Yamaguchi, T., O'Loughlin, F., Neal, J.C., Sampson, C., Kanae, S., Bates, P.D., 2017. A high-accuracy map of global terrain elevations. Geophys. Res. Lett. 44 (11), 5844–5853.

Yan, X., Akiyama, H., Yagi, K., Akimoto, H., 2009. Global estimations of the inventory and mitigation potential of methane emissions from rice cultivation conducted using the 2006 Intergovernmental panel on climate change guidelines. Global Biogeochem. Cycles 23 (2).

Zhang, G., Xiao, X., Dong, J., Xin, F., Zhang, Y., Qin, Y., Doughty, R.B., Moore, B., 2020. Fingerprint of rice paddies in spatial–temporal dynamics of atmospheric methane concentration in monsoon Asia. Nat. Commun. 11 (1), 1–11.